FLOW WITH IMPORTANT HEAT TRANSFER AND/OR COMBUSTION

Experimental Characterization and Modeling of Hazards: BLEVE and Boilover
Small Scale Boilover Experiments

Delphine Laboureur

Environmental and Applied Fluid Dynamics Department, von Karman Institute for Fluid Dynamics, Belgium, laboureu@vki.ac.be

Supervisor & University Supervisor: Jean-Marie Buchlin

Professor, Head, Environmental and Applied Fluid Dynamics Department, von Karman Institute for Fluid Dynamics, Belgium, buchlin@vki.ac.be

Professor, Faculté des Sciences Appliquées, Université Libre de Bruxelles, buchlin@vki.ac.be

Co-Supervisor: Patrick Rambaud

Associate Professor, Environmental and Applied Fluid Dynamics Department, von Karman Institute for Fluid Dynamics, Belgium, rambaud@vki.ac.be

Abstract

Boilover is defined as a violent ejection of fuel due to the vaporization of a water sub-layer, resulting in an enormous fire enlargement and formation of fireball and ground fire. Small scale field and laboratory experiments are performed to allow a better understanding of the characteristics of the pool fire in steady conditions and at the boilover onset.

Keywords: boilover, flame, temperature, burning rate

1. Introduction

Most of the time, hydrocarbon storage reservoirs in process plant sites contain a water layer due to condensation effects, drilling and transport or from the natural composition of the oil. As the water density is higher than most of the hydrocarbons, the water always fall in the bottom of the tank where it is more difficult to remove. If by accident, a fire starts at the fuel surface, this fire progressively heats the fuel layer and therefore the water layer. As the water is heated it starts to vaporize and the vapor generated ejects the fuel from the reservoir. This phenomenon, called boilover, induces violent fuel ejections, flame enlargement and possible formation of fireballs.

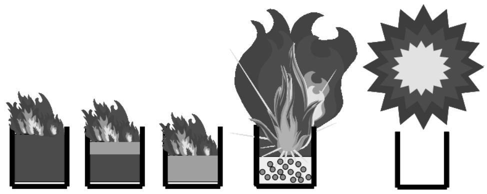

Figure 1: Boilover principle

In 1995, Hua divided the Boilover phenomenon in different steps, from the ignition of the fuel surface to the end of the fuel burning after the Boilover [1]. After ignition of the fuel surface and a small induction period, the pool fire is burning in a regular way, similar to a pool fire without any water sub-layer; the flame is stable and the fire properties like the burning rate or the flame size are constant. Therefore, Hua qualified this period as quasi-steady. During this period, the fuel layer is progressively heating the water layer under it. Once the water layer temperature is getting close to the boiling point, the boilover period starts. Water bubbles develop at the fuel - water interface, and some are ejected through the fuel layer in the flame, emitting a typical crackling sound. Once the water boiling is strong enough to push the fuel layer, the flame height increases quickly and burning fuel is sprayed out of the tank.

Boilover experiments with diesel as fuel, at large scales (reservoir diameter ranging from 1.5 to 6m) have been performed by Munoz and Ferrero [2; 3; 4]. They investigated the pool fire characteristics during the quasi-steady state, but also the change in characteristics from the quasi-steady to the boilover period. In an attempt to compare existing models of pool fire characteristics during the quasi-steady period with different scales of experiments, small scale experiments have been performed in this study.

Garo and Hua [5; 1] performed visualizations of the fuel and water layers and showed that bubbles appear at the fuel - water interface, and increase in scale and in generation rate with time up to Boilover apparition. But very few studies are dedicated to the characterization of the flame enlargement resulting from the piston effect. Therefore, high-speed visualization of the flame enlargement during small scale boilover experiments are also performed.

Figure 2: BABELs experimental facility

2. Experimental apparatus and technique

As boilover experiments include important flame dimensions and fuel projections, a dedicated boilover experimental setup, the BABELs facility, was constructed in beginning 2010 at the von Karman Institute. All the experiments presented in this study have been performed in this facility. After a more detailed description of BABELs, an instrumentation overview is presented.

2.1. Laboratory experimental facility

BABELs is an acronym for Bleve And Boilover ExperimentaL setup (see Fig. 2) and consists of a cylindrical chamber of 2m diameter, and 3m high, with round shape extremities, made out of steel with a rated pressure of 5 bar (hydraulic test). It has 3 series of 7 optical accesses of 0.15m in diameter, separated by 90°, and a door of $0.57m \times 0.77m$. The setup allows air venting through openings in its bottom and upper parts, the last one being ended by a vent that can be used after each test to remove smoke from the chamber. It also contains a ladder and a circumferential walking area at mid-height for better accessibility of the upper optical accesses.

2.2. Experiments overview

In these experiments, the influence of the fuel layer thickness and the ratio between water and fuel layer thicknesses were tested. The influence of the reservoir diameter and material were also investigated by using different reservoirs. Each configuration was performed twice for repeatability check. The fuel used was a mixture of Valvata Shell 460 oil (30% volume) and diesel (70% volume). Oil was added in order to increase the fuel viscosity (favorable condition for boilover apparition [6]). The dimensions and material of the reservoirs (i.e. diameter and height as the thickness is fixed to 2mm in all reservoirs) and the water and fuel layers are listed in Table 1. The glass reservoir was a DURAN crystallizing dish and the metal reservoir was made with steel.

Table 1: Laboratory tests configurations

D [m]	**H [m]**	**Material**	$H_f/D[-]$	H_w
0.08	0.045	glass	$0.1, 0.2, 0.4$	$H_f/H_w = 3$
0.08	0.045	glass	$0.1, 0.2, 0.4$	$H - H_w = 6$
0.08	0.045	metal	$0.1, 0.2, 0.4$	$H_f/H_w = 3$
0.08	0.045	metal	$0.1, 0.2, 0.4$	$H - H_w = 6$
0.15	0.065	metal	$0.1, 0.2, 0.4$	$H_f/H_w = 3$
0.15	0.065	metal	$0.1, 0.2, 0.4$	$H - H_w = 6$

The instrumentation that have been used for the small scale boilover experiments is presented in Fig. 3. For each experiment, mass loss, fuel and water layer temperatures, flame radiation and flame visualization were monitored.

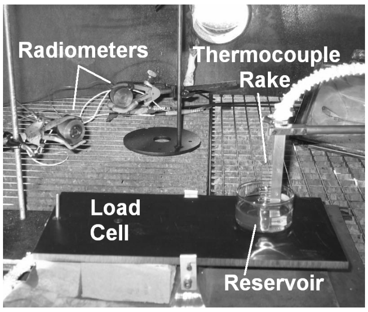

Figure 3: Schematic of boilover experimental setup

2.3. Temperature measurement

The time evolution of the fluid temperature was recorded at different heights from the fuel surface with a thermocouple rake inserted in the reservoir (see Fig. 3). The rake was composed of a series of 26 type K thermocouples of 1mm diameter, sheathed with stainless steel AISI310 and an isolated junction. They were placed together inside two steel clamps of 140mm high, 15mm long and 10mm large, with a thickness of 2mm, acting like a vice (see Fig. 4). The position of the thermocouples were chosen for the best space efficiency, considering the different configurations to be tested: with a space resolution ranging from 1 to 5mm. For the measured temperature to be independent from the clamps, the thermocouple junction were placed out of the support by 10mm length. The part of the 600mm long sheathed thermocouple that was not protected by the vice was surrounded by a silica fiber braided spaghetti from Omerin. The thermocouples were connected to extension thermocouple cables of 3m, that reached a NI9213 acquisition module, plugged in National Instrument Compact-DAQ NI9178 and sampled at 10Hz.

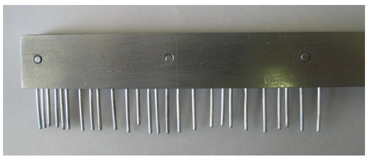

Figure 4: Thermocouple rake

2.4. Mass loss measurement

Simultaneously with the temperature, the mass loss due to the fuel combustion was monitored by a Futek LSB303 load cell with a maximum output of 5kg and a resolution of 0.2g and sampled at 10Hz by using a NI9205 acquisition module. The load cell was compensated on temperature in the $15 - 72°C$ range.
The load cell was fixed between two plates of 150mm large and 300mm long, linked together with a cone-point support. On one side of the cone, the load cell was inserted between the two plates and on the other side, the tested reservoir was placed on the upper plate, made out of Bakelite to reduce the heat transfer from the burning reservoir to the load cell.

2.5. Flame visualization and contours detection

For flame visualizations, a Panasonic NV-GS400 camera was used with a Raynox HD 3035 Pro Semi-Fisheye. The fisheye was needed because of the strong flame enlargement during boilover (up to 2-3m) compared to the distance between the flame and the optical accesses, as imposed by the design of BABELs (1.3m). The distortion created by the fisheye was corrected with Matlab algorithms of image spatial transformation, based on a calibration image representing a check-board (see Fig. 5). Flame visualizations at boilover apparition were also performed with a Phantom V7.1 high-speed camera and a 12mm objective, using an acquisition frequency of 900Hz and an exposure time of $10\mu s$. The fisheye was also used to widen the field of view.

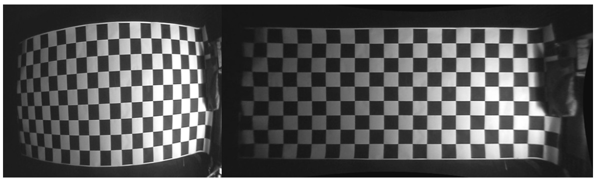

Figure 5: Image calibration: Original image (left) and distorted image (right) (distance between dot = 100mm)

A flame detection algorithm was developed with Matlab Image Processing Toolbox, consisting in several steps. First, a median filter is applied on the images for reduction of possible noise. Then, the image intensity values are adjusted such that only 1% is saturated at low and high intensities, which increases the image contrast. This step is specially needed at beginning of boilover when the flame is very intense, and can cause halo on the images. The resulting gray scale images are converted in binary image, using a global image thresholding based on Otsu method [7]. The pixels on the edges of the flame are extracted by means of the Moore-Neighbor tracing algorithm modified by Jacob's stopping criteria [8]. The computation of flame area, length or width is then straightforward. The definition of flame length differs, depending if the flame is taken from the steady period or during boilover apparition. Both situations are explained later in this article.

3. Steady burning analysis

The characteristics of a diesel pool fire during the quasi-steady period that lasts from ignition to the Boilover apparition are compared with models available in literature when existing. A parametric analysis is also performed, investigating the effect of parameters like the fuel layer thickness or the reservoir diameter on the quasi-steady burning characteristics.

3.1. Burning rate

After ignition of the diesel mixture and a small induction period needed to reach a quasi-steady state, the mass loss becomes constant with time as fuel is burning. The burning rate can then be computed from the slope of the mass loss measurements. A preliminary analysis of the results showed that the burning rate is influenced by the pool diameter, material and by the distance between the top of a vessel and the fuel surface (called lip height).

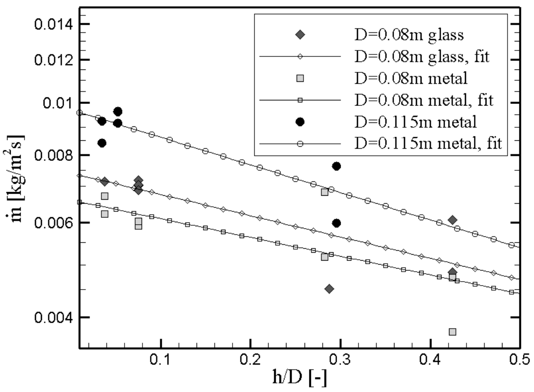

Figure 6: Influence of lip height on burning rate

While the pool diameter effect on the burning rate has been widely studied [9; 10; 11], few papers have dealt with the lip height effect. In 2000, based on an experimental campaign, Dlugogorski [12] has showed that the relationship between the fuel burning rate and the lip height initially follows an exponential decline, as expressed in Eq. 1.

$$\dot{m} = \dot{m}_t exp(-\alpha h^*) \qquad (1)$$

where $\dot{m}_t$ is the burning rate when the liquid level corresponds to the burner rim, α is a fitted parameter and $h^* = h/D$ is the lip height ratio with the vessel diameter [12]. The experimental burning rates confirm the Dlugogorski correlation, as shown in Fig. 6.
A difference is also observed between the burning rates of metal and glass reservoirs. When the material conductivity increases, the burning rate decreases. Indeed, keeping the pool diameter constant, $\dot{m}_t = 7.4 \cdot 10^{-3} kg/m^2s$ for glass reservoir against $6.6 \cdot 10^{-3} kg/m^2s$ for metal reservoir, which gives approximately 10% decrease. This conclusion is in accordance with the previous studies, resumed in Hall [13].

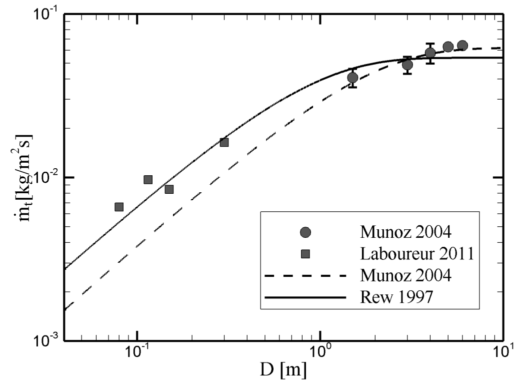

Figure 7: Diesel pool fire burning rate for different pool diameters

Following the Hottel classification of flame regimes, the experiments are ranged in the transition mode, characterized by an increase of the burning rate with the reservoir diameter [9]. The Fig. 7 presents the $\dot{m}_t$ values from the exponential fits of Fig. 6 for a metal reservoir, added with previous results using the same fuel but larger reservoir sizes (D=0.15m and 0.3m [14]). The data fit well the correlation given by Rew [11] (Fig. 7), expressed in Eq. 2, the values of the parameters being listed in Table 2.

$$\dot{m}_t = \dot{m}_\infty(1 - exp(-kD)) \qquad (2)$$

In 2004, Munoz has measured the burning rates of diesel fires from 1.5 to 6m diameter, and proposed a new correlation based on these measurements [2] (see Table 2 for parameters values). But compared to the present experiments, the correlation of Munoz is underestimating the burning rate. This can be due to the oil addition in small scale experiments, or to the influence of conductivity due to the smaller size of reservoir. But putting aside these differences, the correlation of Rew shows a good agreement at the two scales (small scale from the current results and large scale from Munoz [2]).

Table 2: Burning rate correlation coefficients (Diesel oil)

Author	m_∞ $[kg/m^2s]$	k $[m^{-1}]$
Rew	0.054	1.3
Munoz	0.062	0.63

3.2. Temperature profiles

The experimental campaign allowed the measurement of the time evolution of a vertical profile at the center of the reservoir. The following paragraphs are investigating the effect of different parameters on the temperature evolution: the fuel layer thickness, the water layer thickness, the reservoir diameter and the reservoir material.

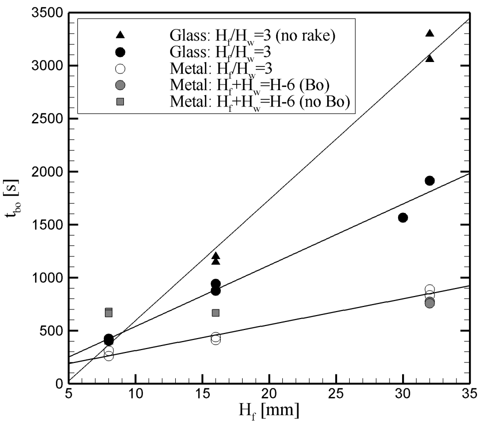

Figure 8: boilover apparition time D=80mm

The Figure 8 presents the boilover apparition time, calculated as the time interval between ignition of the fuel layer surface and the onset of fuel ejection by the water boiling. The presence of the thermocouple rake is clearly accelerating the heating of the fuel and water layers, especially in the glass reservoir. But as the rake is present in all the configurations, a parametric analysis is still possible.

3.2.1. Influence of fuel layer thickness

Figure 9 shows the vertical temperature profile at three fractions of the total time before boilover apparition, for three different fuel layer thicknesses. The fuel layer is more strongly heated as the thickness is decreasing. The influence of the fuel layer thickness on the boilover apparition time is linear, as observed in Fig. 8, which is consistent with previous studies

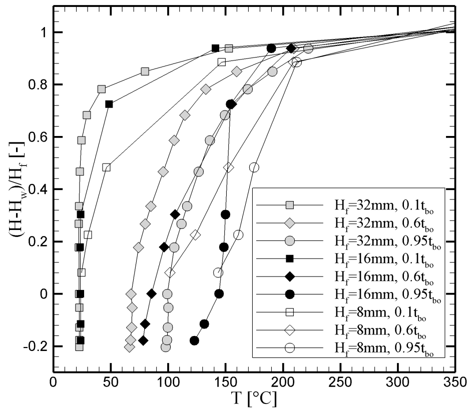

Figure 9: Influence of H_f: D=80mm, metal reservoir, $H_f/H_w = 3$

([15; 16]).

3.2.2. Influence of water layer thickness

The Fig. 10 shows vertical profiles at three different fractions of the time to boilover. The two experiments presented in Fig. 10 have a fuel layer thickness of 16mm and the water layer thickness is either 23mm or 6mm. The influence of the water layer thickness is negligible at the beginning of the combustion, and as the burning time increases, the cooling effect of a thicker water layer becomes more and more visible on the temperature profiles.

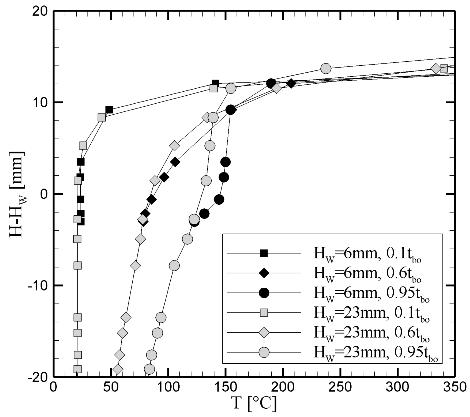

Figure 10: Influence of H_w: D=80mm, metal reservoir, $H_f = 16mm$

But in the case of the large water layer thickness ($H_w = 23mm$), the boilover did not occur; the water layer being too thick to generate the boiling front, causing the piston effect and therefore the flame enlargement. As observed in Fig. 11, if the water to fuel

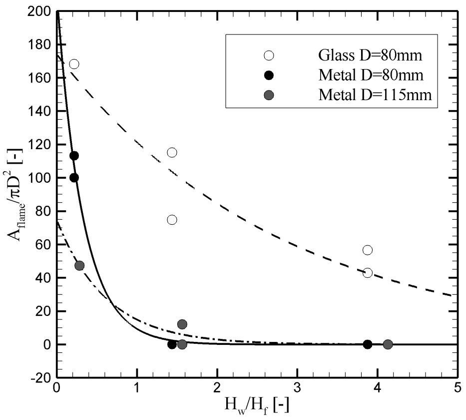

Figure 11: Maximum flame area during boilover occurence

layer thickness ratio is too large, the pool fire extinguishes before the boilover apparition (characterized here by the maximum flame area during boilover). The water layer thickness effect is also visible on the boilover apparition time (Fig. 8). For a small fuel layer thickness, if the water layer thickness is small, the boilover appears quite rapidly. If the water layer thickness is large, the fire extinguishes instead of a boilover apparition, and happens after a larger time. And for small water to fuel layer thickness ratio, a smaller water layer thickness decreases the boilover apparition time.

3.2.3. *Influence of reservoir material*

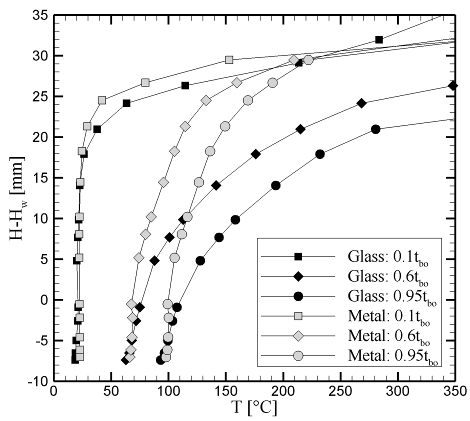

Figure 12: Influence of reservoir material: D=80mm, $H_f = 32mm$, $H_f/H_w = 3$

The Fig. 12 illustrates the influence of the reservoir material on the fuel heating. The heating of the water layer is similar for both materials, but the heating of the fuel layer is a lot stronger in the glass reservoir. This is due to the conduction inside the walls of the reservoir, which is more pronounced with a metal reservoir than with a glass. This can also explain the difference in the time for boilover apparition (see Fig. 8). As there is few conduction inside the walls of the glass reservoir, the water layer is heated only by the conduction and radiation propagated by the combustion, which takes more time than if there is conduction inside the walls (like with the metal reservoir).

3.2.4. *Influence of reservoir diameter*

The influence of the reservoir diameter on the temperature profiles can be observed in Fig. 13. The effect of the diameter on the fuel and water layers is similar than the effect of the material: there is almost no change on the heating of the water layer as the diameter increases, but the heating of the fuel layer is stronger for the larger reservoir.

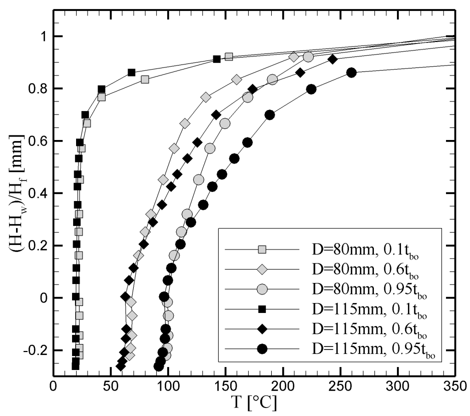

Figure 13: Influence of reservoir diameter: Metal reservoir, $H_f/D = 0.4$, $H_f/H_w = 3$

This is again due to the conduction inside the walls of the reservoir, which has a smaller effect on the liquid when the reservoir size increases. Concerning the boilover apparition time, for two diameters of $D = 80mm$ and $D = 115mm$, with the same fuel layer over diameter ratio ($H_f/D = 0.4$), the time increases from around 850sec to 1350sec. This means that, even if the burning rate increases with the diameter (as shown in the previous section), the conduction effect is less pronounced for a larger diameter and increase the boilover apparition time.

3.3. *Flame shape*

Numerous studies are available in literature concerning the pool fire flames characteristics; experimental studies at different scales and fuel types, but also correlations. For each quantity, the main correlations available in literature are compared with experimental data extracted from the flame images recorded with the digital camera and the fish eye.

Figure 14: Mean flame D=115mm,$H_f/D = 0.4$, $H_f/H_w = 3$

Pool fire flames are diffusive and the flame time evolution is oscillatory. The flame can be decomposed in three regions: the base flame, the intermittent flame (where the flame oscillations are visible) and the plume region, at the top. In Fig. 14, representing the average flame during the steady burning, the two first regions are clearly visible. The base region is represented as the small white cone appearing in all images, and the intermittent flame is shown as the larger grey cone. The black line at the left of the flame is due to the presence of the thermocouple rake. The frequency of the oscillations, controlling the rate of air entrainment into the flame has been called the puffing frequency by Weckman [17]. The principal geometrical quantities that define flames from a pool fire are the flame length and tilt. The flame tilt is only function of the wind speed. As in this study the experiments are performed in a calm environment (without wind), only the flame length is investigated here.

3.3.1. *Flame length*

As explained before, pool fire flames oscillate; the flame length is changing with time. In this article, the approach developed by Zukoski [18], and followed by Ferrero [4] is applied. The average flame length is defined as the length at which the intermittency $I(L)$ (which is the fraction of time in which the flame is higher than L), is equal to 0.5. The calculation of flame length intermittency is carried out using MATLAB, based on the processing of 999 images in the steady part of the pool fire (recorded 1 to 2 minutes after ignition). For each image, the flame length is calculated as the distance between the reservoir edge and the upper pixel of the flame profile.

$$\frac{L}{D} = a(m^*)^b(u^*)^c \tag{3}$$

$$m^* = \frac{\dot{m}}{\rho_a \sqrt{gD}} \tag{4}$$

$$u^* = \frac{u}{(\frac{\rho_a}{g\dot{m}D})^{1/3}} \tag{5}$$

Among the correlations that predict the flame length, most of them show a dependency with the diameter, the burning rate and the wind speed, in the form of Eq. 3-5, each model having a specific set of values for the parameters *a*, *b* and *c* and are resumed in Table 3.

Table 3: Flame length correlation coefficients

Author	a	b	c
Thomas [19]	42	0.61	-
Moorhouse [20]	4.7	0.21	-0.044
Mangialavori [21]	31.6	0.58	-
Ferrero [4]	4.201	0.181	-0.082

The Fig. 15 compares the average flame length for the different configurations tested in this study, with previous experimental data showed by Mudan and Ferrero [22; 4] and the correlations of Thomas (considering no wind) [19], Moorhouse (with a conical flame shape) [20], Mangialavori [21] and Ferrero [4]. For the measurements of this study, the burning rates used in Eq. 4 are determined from the exponential fits following the Dlugogorski model (see Fig. 6). The correlation the closest to the experiments is the one of Mangialavori [21]; the correlation of Thomas [19] showing a similar trend, but with an overestimation.

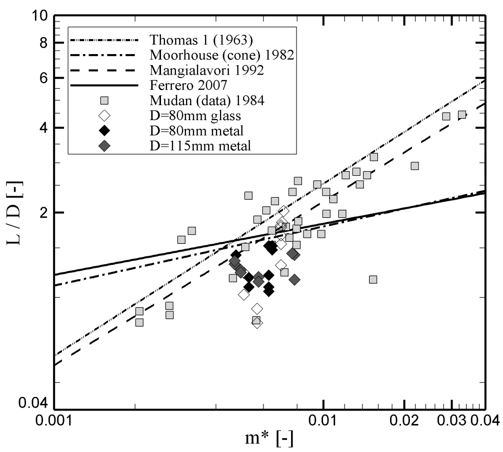

Figure 15: Flame length, compared with other data and correlations

3.3.2. Flame frequency

Following the approach of Ferrero [4], the flame frequency is calculated from the time evolution of the flame height. The approach of Ferrero [4] consists in first, to smooth the signal and then to calculate the puffing frequency as the ratio between the number of peaks in the flame length signal, divided by the average time duration of one oscillation. But as each pool fire configuration has its own set of 999 images, the length of the signal used here is too long to apply the procedure of Ferrero [4]. So another approach is to calculate the FFT of the signal. But Henriksen [23] has explained that, due to the turbulent nature of the flame, the FFT is too noisy to identify clearly the frequency peak. Therefore, the Burg implementation of the maximum entropy method to calculate the power spectrum is used, which gives a lot smoother results than the traditional FFT approach.

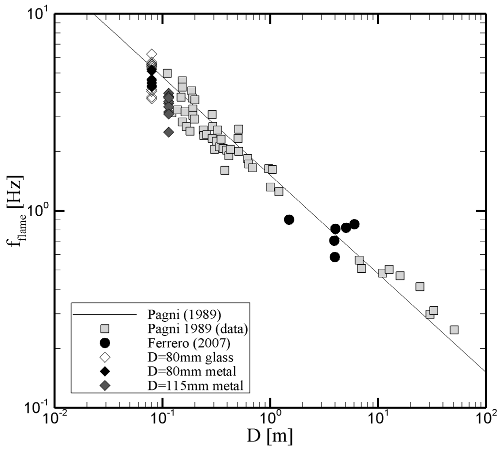

Figure 16: Flame flickering frequency, compared with other data and correlation of Pagni [24]

The Fig. 16 shows the resulting puffing frequencies, compared with the correlation of Pagni [24], which has the form of Eq. 6, the data presented by Pagni [24] in the same article, and the data of Ferrero [4]. The experiments of the present study show the same discrepancy as the previous experimental data, and follow the correlation.

$$f = \sqrt{\frac{2.3}{D}} \qquad (6)$$

4. Boilover analysis

4.1. Pre-boilover burnt mass ratio

The ratio between the fuel mass burnt before the occurrence of boilover and the initial fuel mass is an important parameter since it provides information on the available quantity of fuel that can be ejected during the water boiling. In previous studies, Garo and Ferrero [5; 3] showed that the pre-boilover burned mass ratio (also called χ) depends both on the initial fuel thickness and on the pool diameter. They presented either an evolution of χ with the fuel thickness, or with the pool diameter, but no attempt to combine the effect of the two parameters was done.

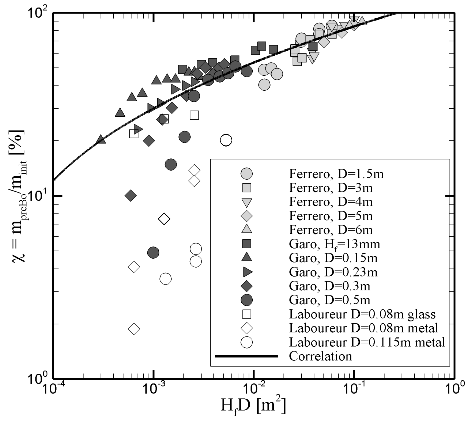

Figure 17: New correlation for the pre-boilover burnt mass ratio χ

The Fig. 17 presents the pre-boilover burnt mass ratio in function of the product of the initial fuel layer thickness and the pool diameter. The data of the present experiments (white points) are presented together with the previous results of Garo (using heating oil, dark grey points [5; 15]) and Ferrero (using diesel, light grey points [3]). The correlation in the form of a power law (see Eq. 7) follows well the large and middle scale. A discrepancy is observed only at smaller scale.

$$\chi = 170.3\left(H_f D\right)^{0.1171} - 45.81 \qquad (7)$$

This is probably due to the influence of the wall conduction in the heating process of the small scale reservoir, which is not present at larger scales. Indeed, the glass reservoir points of this study are following a lot better the correlation than the metal reservoir points, as glass is not a good heat conductor.

4.2. Flame enlargement

The major boilover hazard is the flame enlargement resulting from the piston effect induced by the water boiling, as observed from high-speed visualization performed in a previous study [25]. A typical flame enlargement recorded with the high-speed camera is shown in Fig. 18. The water boiling front is first pushing the fuel in the flames, which enhances the combustion and increases the flame size to form a fireball shape which evolves into a column. Once the water boiling stops, the flame decreases and comes back to its original flame size or extinguishes, depending on the remaining quantity of fuel. If the whole fuel layer is not participating to the flame enlargement, several boilover can be observed.

Figure 18: Flame enlargment during boilover apparition (D=115mm metal reservoir, $H_f/D = 0.2$), $\Delta t = 0.11s$ between images

The LS-PIV technique (Large Scale Particle Image Velocimetry) that calculates the flow velocity based on large structures instead of individual particles, can be used by processing the high-speed flame images with an algorithm for the interrogation of PIV images, based on cross-correlation [26].

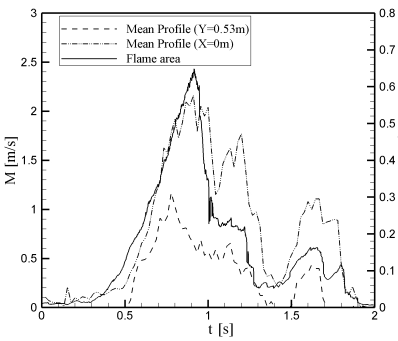

Figure 19: Flame velocity compared with total area (D=115mm metal reservoir, $H_f/D = 0.2$)

In Fig. 19, the time evolution of a vertical velocity profile at the center line of the reservoir is compared with the time evolution of an horizontal profile at about $4.6D$ above the reservoir, and with the total flame area calculated with the flame detection algorithm explained previously.

Once the fuel is ejected from the reservoir, both the flame size and velocity magnitude are increasing in a similar way until reaching a maximum flame size

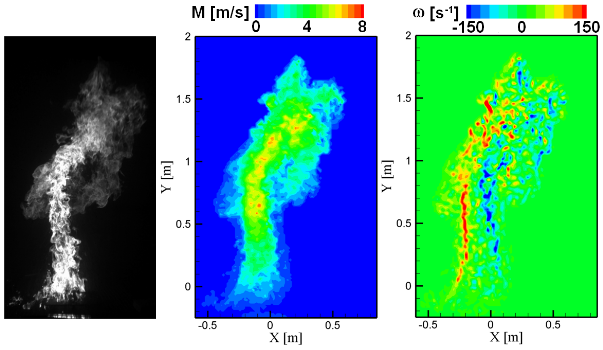

Figure 20: Max area (D=115mm metal reservoir, $H_f/D = 0.2$), t=0.91s after Boilover onset

around $t = 0.91s$. The Fig. 20 shows the velocity and vorticity fields at the time of the maximum flame area. It can be observed in the velocity field that the movement of the flame is mainly coming from the flame center line and from the vorticity field, shear is visible on the flame boundary.

After reaching the maximum area, the flame size is decreasing until reaching almost its original size. A second smaller peak is visible on the area and velocity plots (after $t = 1.5s$). This is not a second boilover but more a ground fire aside of the reservoir created by the ejection of fuel during the boilover. In Fig. 19, a second peak in the velocity evolution is visible, while the flame size is decreasing. The Fig. 21, representing the flame at the second velocity peak ($t = 1.2s$) shows that, even if the flame is smaller, the upper part is moving faster than the larger flame. In addition, the shear is increased.

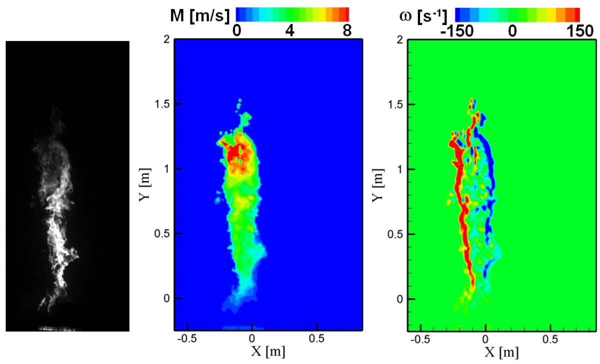

Figure 21: 2nd peak of velocity (D=115mm metal reservoir, $H_f/D = 0.2$), t=1.2s after Boilover onset

The general correlation between the flame size and velocity has already been observed and different authors have proposed a relationship between the flame height and the Froude number which is a measure of the relative importance of inertia and buoyancy [27; 28; 29]. In an attempt to find a correlation independent on fuel type, Zukoski [27] have expressed the square root of a Froude number in terms of the heat release rate (see Eq. 8-9 [30]).

$$\dot{Q}_D = V\Delta H_c \rho_{fv} \left(\pi D^2/4\right) \tag{8}$$

$$\dot{Q}_D^* = \frac{\dot{Q}_D}{\rho_a C_{p_a} T_a \sqrt{gD} D^2} \tag{9}$$

Depending on the value of $\dot{Q}_D^*$, the flame can be momentum or buoyancy dominated. The time evolution of $\dot{Q}_D^*$ is calculated for the boilover phenomenon, using as the velocity V, an average of the vertical velocity along the horizontal profile just above the reservoir.

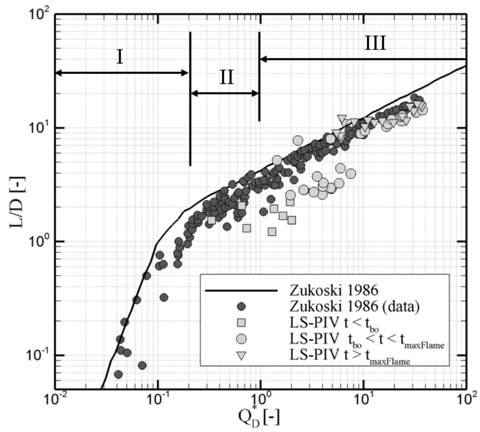

Figure 22: Flame length evolution with non dimensional Froude number

Before the apparition of the boilover (light grey squares in Fig. 22), the flame height is in the buoyancy dominated region II, dependent both on the heat release rate and the pool diameter [27]. Delichatsios defines also the interval $0.23 < \dot{Q}_D^* < 1.9$ as typical for intermediate scale pool fire [31]. During the boilover (light grey circles and diamonds in Fig. 22), the flame height increases to the region III, where the dependency on the pool diameter is negligible compared to the heat release rate. Delichatsios defines flames with $\dot{Q}_D^* > 1.9$ as buoyant jet flames [31]. This regime is consistent with the boilover phenomenon, since the velocity and the flame size are increasing while the reservoir size is kept constant. In addition, an increase of $\dot{Q}_D^*$ is similar to an increase of the Froude number, and therefore a stronger importance of the momentum, created by the piston effect of the water boiling, compared to the buoyancy, which is normally dominant for this pool fire configuration. And when the boilover ends, the flame comes back to the regime II, as before the boilover apparition.

5. Conclusion

A small scale experimental campaign have been performed, allowing the selection of the best correlation from the previous studies available in literature, for diesel pool fires of small to large scale. The fuel burning rate for a completely filled reservoir can be well predicted by Rew [11] and the influence of the lip height on the burning rate, first pointed by Duglogorski [12] has been proved. The temperature evolution of the fuel and water layer is influenced by the pool diameter and material, but also by the fuel and water layer thickness. Conduction through the walls of a metal reservoir is heating the fuel and water layers faster, which accelerates the boilover apparition. The conduction effect is decreased as the reservoir diameter increases. Conduction can also prevent boilover from happening when the water layer is at least two times bigger than the fuel layer, acting like a heat sink. As no hot-zone have been observed, the boilover apparition time is increasing with the fuel layer thickness, as already observed by Garo and Koseki [15; 16]. Finally, the best correlation for the average flame length is given by Mangialavori [21] and the flame puffing frequency during the steady period can be correctly modeled by Pagni [24].

The small scale experiments have also improved the understanding of the flame enlargement during the boilover period. A new model for the pre-boilover burnt mass ratio, which is directly linked to the boilover intensity, is proposed, which takes into account both the fuel thickness and the reservoir diameter. This new correlation works fine when the conduction through the reservoir wall is limited. The flame enlargement during boilover has been visualized by high-speed camera and processed with a PIV algorithm that allowed to compute the flame velocity. During a boilover, the flame velocity and size are increasing and decreasing with time with the shape of a Gaussian. By using a dimensionless parameter for the velocity (changed into a dimensionless heat release rate linked to the Froude number) and for the flame length (using the pool diameter), the buoyancy dominated flame typical of medium size pool fire is turning during boilover into a jet flame, where only the velocity of the flame is influencing its height, before coming back to the steady pool fire flame after the boilover.

Nomenclature

ROMAN SYMBOLS

A	Area $[m^2]$
a, b, c	Constants in flame length model
C_p	Specific heat $[kJ/kgK]$
D	Pool diameter $[m]$
ΔH_c	Heat of combustion $[kJ/kg]$
f	Puffing frequency $[Hz]$
g	Gravity $[m/s^2]$
h	Lip height $[m]$
H	Height $[mm]$
k	Extinction coefficient $[m^{-1}]$
L	Flame length $[m]$
m	Mass $[kg]$
$\dot{m}$	Burning rate $[kg/m^2 s]$
M	Velocity magnitude $[m/s]$
$\dot{Q}_D$	Heat release rate $[kW/m^2]$
t	time $[s]$
T	Temperature $[°C]$
u	Wind speed $[m/s]$
V	Vertical flame velocity $[m/s]$
X	Horizontal coordinate $[m]$
Y	Vertical coordinate $[m]$

GREEK SYMBOLS

α	Constant in Dlugogorski model [-]
Δt	Time interval $[s]$
ρ	Density $[kg/m^3]$
χ	Pre-boilover burnt mass ratio [%]
ω	Vorticity $[s^{-1}]$

SUBSCRIPT

a	Air
bo	Boilover onset
f	Fuel
fv	Fuel vapor
$flame$	Flame
$init$	Before ignition
$preBo$	Before Boilover onset
t	No lip height
w	Water
∞	Infinite diameter
$*$	Dimensionless

Acknowledgments

The authors wish to thank the CEA of Gramat which is supporting this study and collaborating with the von Karman Institute and the Ecole des Mines d'Alès in this joint research project about source term characterization in major hazards.

References

[1] J. Hua, W. Fan, G. Liao, Study and prediction of boilover in liquid pool fires with a water sublayer using micro-explosion noise phenomena, Fire Safety Journal 30 (3) (1998) 269–291.

[2] M. Munoz, J. Arnaldos, J. Casal, E. Plana, Analysis of the geometric and radiative characteristics of hydrocarbon pool fires, Combustion and Flame 139 (3) (2004) 263–277.

[3] F. Ferrero, M. Munoz, B. Kozanoglu, J. Casal, J. Arnaldos, Experimental study of thin-layer boilover in large-scale pool fires, Journal of Hazardous Materials 137 (3) (2006) 1293–1302.

[4] F. Ferrero, M. Munoz, J. Arnaldos, Effects of thin-layer boilover on flame geometry and dynamics in large hydrocarbon pool fires, Fuel Processing Technology 88 (3) (2007) 227–235.

[5] J. Garo, Combustion d'hydrocarbures répandus en nappe sur un support aqueux. analyse du phénomène de boilover, Ph.D. thesis, Université de Poitiers, Faculté des Sciences fondamentales et appliquées (1996).

[6] K. Hasegawa, Experimental study on the mechanism of hotzone formation in open tank fires, Proc. Fire Safety Science, 2nd Int. Symp. (1987) 221–230.

[7] N. Otsu, A threshold selection method from gray-level histograms, IEEE transactions on systems, Man and Cybernetics 9 (1) (1979) 62–66.

[8] R. Gonzalez, R. Woods, S. Eddins, Digital image processing using matlab, New Jersey, Pearson Prentice Hall.

[9] H. Hottel, Review: certain laws governing the diffusive burning of liquids, by blinov and khudiakov, Fire Res. Abstr. Rev. 1 (1959) 41–44.

[10] V. Babrauskas, Estimating large pool fire burning rates, Fire Technology 19 (1983) 251–261.

[11] P. Rew, W. Hulbert, D. Deaves, Modelling of thermal radiation from external hydrocarbon pool fires, Safety Environ. Protect. 75 (1997) 81–89.

[12] B. Dlugogorski, M. Wilson, Effect of ullage on properties of small-scale pool fires, Dev. Chem. Eng. Mineral Process. 8 (1/2) (2000) 149–166.

[13] A. Hall, Pool burning, Oxydation and Combustion Rev. 6 (1973) 169–225.

[14] D. Laboureur, Experimentation a petite echelle du phenomene de boilover, Actes du Congres Annuel de la SFT 18 (2) (2010) 345–350.

[15] J. Garo, H. Koseki, J. Vantelon, C. Fernandez-Pello, Combustion of liquid fuels floating on water, Thermal Science 11 (2) (2007) 119–140.

[16] H. Koseki, M. Kokkala, G. Mulholland, Experimental study of boilover in crude oil fires, Proceedings of the 3rd International Symposium of Fire Safety Science (1991) 865–874.

[17] E. Weckman, A. Sobiesiak, The oscillatory behavior of medium scale pool fires, 22nd Symposium (International) on Combustion 180 (4) (1988) 699–712.

[18] E. Zukoski, B. Cetegen, T. Kubota, Visible structure of buoyant diffusion flames, 20th Int. Symp. on Combustion 20 (1) (1985) 361–366.
[19] P. Thomas, The size of flame from natural fires, 9th Symposium on Combustion, Pittsburgh (1963) 844–859.
[20] J. Moorhouse, Scaling criteria for pool fires derived from large-scale experiments, IChemE Symposium Series 71 (1982) 165–179.
[21] G. Mangialavori, F. Rubino, Experimental tests on large hydrocarbon pool fires, 7th International Symposium on Loss Prevention and Safety Promotion in the Process Industries, Italy.
[22] K. Mudan, Thermal radiation hazards from hydrocarbon pool fires, Progress in Energy and Combustion Science 10 (1) (1984) 59–80.
[23] T. Henriksen, T. Ring, E. Eddings, G. Nathan, Puffing frequency and soor extinction correlation in jp-8 and heptane pool fires, Combustion science and Technology 22 (1) (2008) 1299–1310.
[24] P. Pagni, Pool fire vortex shedding frequencies, in some answered questions in fluid mechanics, Applied Mechanics Review 43 (8) (1989) 153–170.
[25] D. Laboureur, Experimental characterization and modeling of hazards: Bleve and boilover, Summaries of VKI's doctoral candidate research (2011) 145–151.
[26] F. Scarano, Iterative image deformation methods in piv, Measurement science and Technology 13 (1) (2002) R1–R19.
[27] E. Zukoski, Fluid dynamic aspects of room fires, Proc. Fire Safety Sicence, 1st Int. Symp. (1986) 1–30.
[28] G. Heskestad, Luminous heights of turbulent diffusion flames, Fire Safety Journal 5 (2) (1983) 103–108.
[29] M. Delichatsios, Transition from momentum to buoyancy-controlled turbulent jet diffusion flames and flame height relationships, Combustion and Flame 92 (4) (1993) 349–364.
[30] D. Drysdale, An introduction to Fire Dyanmics, second edition, John Wiley & Sons, West Sussex, England, 1999.
[31] M. Delichatsios, Air entrainment into buoyant jet flames and pool fires, Combustion and Flame 70 (1) (1987) 33–46.

Shape and Temperature Field Distortions Induced by Convective Effect on Hot Object in the Visible, near Infrared and Infrared Bands

Anthony Delmas

Environmental and Applied Fluid Dynamics Department, von Karman Institute for Fluid Dynamics, Belgium, anthony.delmas@vki.ac.be

Supervisor: Jean-Marie Buchlin

Professor, Environmental and Applied Fluid Dynamics Department, von Karman Institute for Fluid Dynamics, Belgium, buchlin@vki.ac.be

University Supervisor: Le Maoult Yannick

Doctor, Metrology, Identification, Control and Surveillance Department, Institut Clement Ader, France, yannick.lemaoult@mines-albi.fr

---

Abstract

The goal of this study is to point out the perturbation induced by convective effect (mirage effect) on shape and temperature measurement and to give an estimation of the error done. This work will explore the sensitivity of several spectral bands and single wavelengths. A numerical approach is carried out and an original set up has been build in order to investigate easily all the spectral bands of interest with the help of CCD camera (Si) or VisGaAs camera. We will give the displacement due to the perturbation for each spectral band and finally give some hints about how to correct it.

Keywords: high-temperature, mirage effect, natural convection, infrared, near infrared, visible, hot disk.

---

1. Introduction

In industries like in research center, non-contact measurements of the temperature and/or of the displacement are often necessary. A good way to do it is to use cameras and to observe the object whom we want to know size and temperature. Some studies has been done in order to use usual visible CCD cameras (Silicium detector 0.35μm-1.1μm) to make thermal-dimensional coupling measurements and merge usual video data with infrared data [1]. Several advantages to work in the near infrared to measure the temperature exist, for instance, we have a good sensibility and well resolute detector and we are less dependent on the unknown emissivity of metals. However, some investigations made in this specific domain have underlines some perturbations emphasized at high-temperature (T≥800°C), the standard deviation of dimensional measurements is multiply by 5 [2]. Numerous works realized by means of camera to provide measurements have pointed out the problem of images pertubated by refractive index gradient in the air [3; 4; 5; 6]. We will focus in this study on perturbations which arise from convective effect present around hot objects. Such perturbation can induce a shape distortions in the visible band but also errors on shape and temperature measurements for near infrared and infrared bands. We choose first to focus on a simple geometry objects like a cylinder or a hot horizontal disk in order to generate a reproducible convective plume. We present here a numerical way (ray-tracing [7]) to obtain the displacement induced by the density variation and an experimental method to get quantitative values of displacements. Because of the recent emergence of new generations cameras with high resolution even in the infrared band, this work will be carry out for several spectral bands going from visible until infrared passing by near infrared. Finally, we will give some ideas about a strategy of correction of pertubated images.

2. Mirage effect: description and generation

The mirage effect appears as soon as we have a refractive index gradient. What we called mirage effect is when light beams do not arrive at the expected destination (without temperature gradient). Usually this effect does not have a big influence on optic measurement. But, if we are in presence of a strong refractive index gradient, the information measured can be wrong enough to be taken into account. In our case, the refractive gradient is engendered by a temperature gradient coming from a natural convective plume. The convection is induced by the movement of molecules within fluids, here the air, due to temperature differences which affect the density, and thus relative buoyancy, of the fluid. More dense components will fall while less dense components rise, leading to bulk fluid movement. In the case of a hot object, the convective field around it will pilot the temperature field around the object. This temperature gradient around and above the object leads to a refractive index gradient which, if the deviation is important, can bring big aberrations. Light distortion induced by natural convection is very frequent and can be observed in numerous cases. The most famous one is the mirage effect which occurs over a road or in the desert when the sun is strongly hitting the ground (Fig. 1).

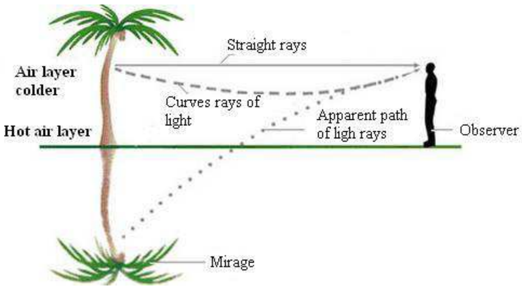

Figure 1: Mirage effect principle.

Either the observed object is far (hundreds of metres) and the deflection can be important even with small gradient (20°C of relative difference), see Fig. 2, or the object is close to the observer (few metres or centimetres) but the temperature gradient is much strong (500°C to ambiant temperature) like in the Fig. 3.

In our case, we will focus on mirage effect occurring within a short distance. It can be sometimes a real problem when we need to know with accuracy the shape or the temperature of a given point of the object. We give in this work a value of the error made when we are trying to make such measurement. In addition, the deflection induced by the temperature gradient varies with the wavelength. According to the Eq. 1 called Gladstone-Dale law [8], we can obtain for a given temperature field and wavelength, the refractive index distribution.

Figure 2: Mirage effect with far object.

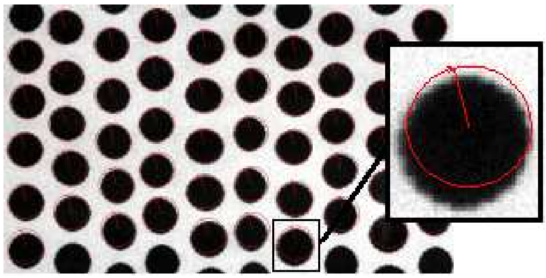

Figure 3: Mirage effect with object 1m far (circles are the original shape of the black disk).

$$n_\lambda - 1 = K_\lambda \cdot \rho(T) \tag{1}$$

$$\text{where } K_\lambda = (N \cdot \alpha_0)/(2 \cdot \epsilon_0) \tag{2}$$

The Gladstone-Dale parameter K is function of the wavelength λ (because α_0: polarizability of one molecule depends on λ), ϵ_0 is the vacuum permittivity and N is the Avogadro number. We choose to work first in the visible band, with the wavelength of the He-Ne laser: λ =632,8nm and K=0,2256.10^{-3} m^3/kg. In our case, air can be taken as an ideal gas, and so:

$$\rho(T) = 352.86/T \tag{3}$$

With combination of Eqs. 1 and 6, we establish for the specific wavelength of an He-Ne laser:

$$n - 1 = 0.079 \cdot T^{-1} \tag{4}$$

We can see in the Fig. 4 how the refractive index depends on the temperature and on the wavelength. The index of refraction decreases with the rise of temperature or wavelength. However, we see that the variation of the refractive index tends quickly to a constant value. The variation is the most important for the short wavelength (UV and visible). Knowing that the bigger the refractive index is, the more the light is deviated, if we look a mirage effect with a visible camera (or by eyes), we will see only the biggest deviation corresponding to the shortest wavelength of the camera (≈400nm). It means that we dont need to use an effective refractive index for a spectral band (refractive index integrated index over the spectral band) to obtain the displacement observed in real but only the one corresponding to the shortest wavelength. Above 1000nm, it doesnt really matter anymore since the refractive index varies very slightly. We are now able to obtain directly from the temperature field, the refractive index distribution for a given wavelength.

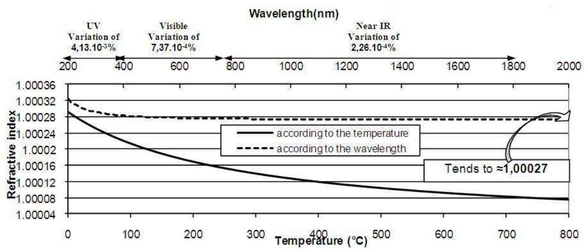

Figure 4: Refractive index evolution according to the wavelength (at 15°C) and to the temperature (at λ=632,8nm) [9].

The next step is now to choose a hot object able to generate a reproducible convective effect with an important temperature and refractive index field. We thought first to use a vertical hot plate but issues appear quite fast about a well homogenized hot plate and the generation of a stabilized boundary layer [10]. Our choice ended on the generation of a plume coming from a hot horizontal disk. This generation of the perturbation is interesting because is a free convection, in agreement with our context, and in addition, such system permits to obtain both a strong displacement of the lights through the perturbation and a heating element of small dimensions. Displacements expected and size of the heating element are both validated thanks to a ray-tracing method and a CFD software (cf. section 3). Moreover, since the heating element is much smaller than a vertical plate, its possible to generate very high temperature with a good homogeneity. We present now how the design of the set-up has been selected.

3. Numerical tool and experimental design

The heating element chosen is a hot horizontal disk generating an axisymmetric plume. We will discuss here which diameter it should have and the temperature necessary to have a displacement big enough to be measured. Firstly, before to start any computation or sizing, we should verify in which regime the flow in the plume will be. In free convection, a non-dimensional number is used as reference to predict the flow regime, its the Rayleigh number:

$$Ra = (g \cdot \beta \cdot \Delta T \cdot x^3)/(a \cdot \nu) \qquad (5)$$

With g gravitational acceleration, β dilatation coefficient, ΔT difference of temperature between the air and the disk, x the characteristic length (diameter of the disk), a the thermal diffusion of the air and ν the cinematic viscosity. We want something small enough to be easily heat up and to have a good homogeneity. If we take a disk with a diameter of 10cm and heated up to 1200K (around the highest temperature of materials met in our laboratory) we obtain a Rayleigh number equal to $2{,}19.10^6$. This means that the flow will never reach a turbulent flow, cause the transition limit between laminar and turbulence is defined at Ra=10^9. With such laminar plume, we have something easily reproducible and well established. We can notice here that such laminar convective flow is the case of almost all the hot objects studied in laboratory (an images average can be needed in order to override external perturbations). In addition, the big advantage of a perturbation generated by such device is the displacement brought throw the plume. Indeed, an axisymmetric perturbation brings, just by its own curved shape, a light deviation (cf Eq. 10). Moreover, the temperature gradient in the plume is really strong (much stronger than a jet of hot air blowing from a pipe), and thus gives another way to deviate efficiently the rays of light. We can now start the numerical simulation of the deflection induced by the plume. The numerical method is described briefly in the Fig. 5. We first need to obtain the temperature field above the disk, to deduce the refractive index from the temperature and to include it in the ray-tracing code. We will present in this paper only the sizing case which gives best results. An insulator will be take into account in the simulation in order to avoid a gradient temperature on the disk surface during the experiment.

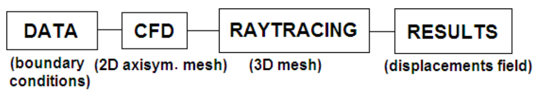

Figure 5: Diagram showing the main steps of the numerical method.

3.1. Computational fluids dynamics (CFD)

3.1.1. Simulation

The first step is to know the temperature field in the plume. We will compute it with the help of a CFD

software. The axisymmetric geometry is meshed with Gambit then introduced in FLUENT (Fig. 6). The computing is, as we showed it upper, realized in laminar flow. Often, in order to facilitate the computation, correlations are used to define the material properties (here the air) [11]. The different correlations used in our case are the followings:
About the density, we know that the air can be assimilate as a perfect gas. The error made compared to the exact values are in average about 0.16% in our temperature scale (300K to 1300K). Thus, the correlation used for the density is the perfect gas law:

$$\rho(T) = (P \cdot M)/(R/cdotT) \tag{6}$$

With ρ the density (kg/m^3), P the pression, M molecular mass, R the perfect gas constant, T the temperature. // For the viscosity, the correlation used is:

$$\mu(T) = 1,875.10^{-5} \cdot (T/273)^{0,6386} \tag{7}$$

For the specific heat:

$$Cp(T) = 975,3 + 0,0368 \cdot T + 2.10^{-4} \cdot T^2 \tag{8}$$

For the thermal conductivity:

$$\lambda(T) = 0,026(T/293)^{0,7231} \tag{9}$$

In this condition, we obtain the temperature field around and above the disk (Fig. 7)

The size of the domain has be taken big enough (50cmx100cm) in order to avoid any kind of border effect. The mesh is made in order to have smaller cells close to the disk. The number of cells in this simulation is 60000 (300 vertically by 200 horizontally).

3.1.2. *Results validation*

The validation of FLUENT results will be carried out in the section 4 and numerical results will be compared with the experimental ones.

3.2. *Ray-tracing*

The ray-tracing code has been initially developed to simulate the heating of plastic preform in the ICA. The code has been modified for our study to be able to make optic computations in an environment of inhomogeneous refractive index.

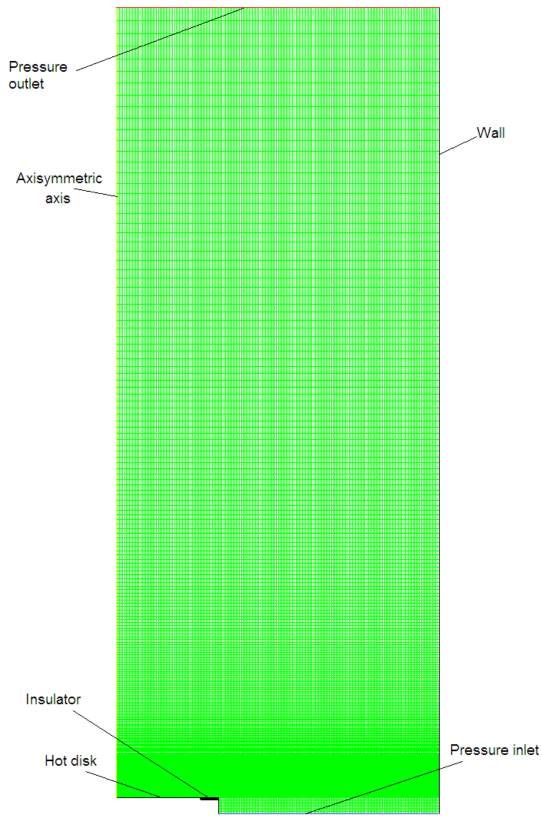

Figure 6: Mesh and boundary conditions used for the simulation.

3.2.1. *Preliminary validation*

In order to validate the ray-tracing code, we will use a simple geometry and we will compare the numerical result with an analytic one. The geometry used here is a vertical plate (see details in Fig. 8) with a uniform index of 3. In order to reduce a maximum errors due to approximation, the air index will be taken equal to 1 numerically and analytically. The ray will be throw from the original plan with a vertical angle α of 1° and 2°.

With this configuration, we find analytically a displacement Z of 4.654mm and 9.311mm respectively for 1° and 2°. The results obtained using the ray-tracing code are respectively 4.654mm and 9.309mm. The error made by the code is inferior to 0.02

3.2.2. *Simulation*

For the input data of the code, thanks to the Gladstone-Dale law (Eq. 4), we deduce from the temperature field, the refractive index field for a given wavelength (for the example we chose λ=632,8nm). Finally, we incorporate this refractive index field in

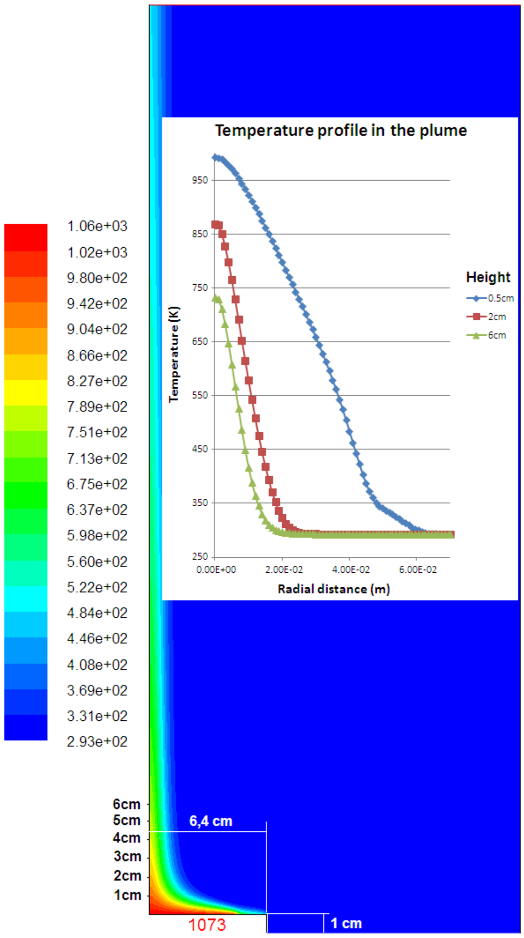

Figure 7: Temperature contours obtained with FLUENT and temperature profiles at different heights above the disk at 1073K.

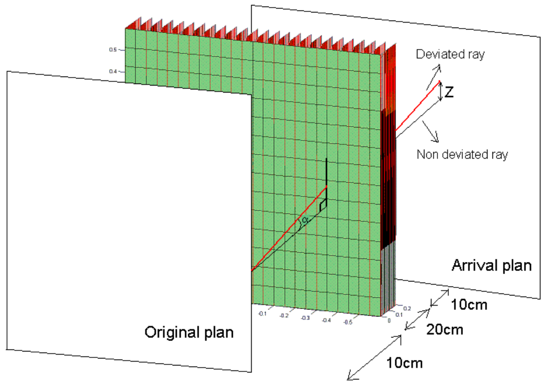

Figure 8: Geometry and distances used for the validation.

our ray-tracing code as the Fig. 9 illustrates it. The original plan is composed of radiating elements located with their y and z coordinates. Each element launches one ray perpendicularly to the original plan. The refractive index field around and above the disk is discretized according to the radial, circumferential and axial coordinates in order to create a large number of cells with constant refractive index (Fig. 10). A parametrical analysis on the mesh has been realized before in order to obtain good results within a time not too large (the creation of 1 000 000 cells (100x100x100) leads to several days of computation [15 days exactly on our computer]). We will choose here a mesh of 125 000 cells (50x50x50), giving a computing time of approximately 6h30 (AMD Opterion 2GHz, 1Mo cache, 2Go Ram, on Linux-Feodora). The error between a meshing of 1 000 000 cells and 125 000 cells is between 10 and 15% but the time saved is consequent.

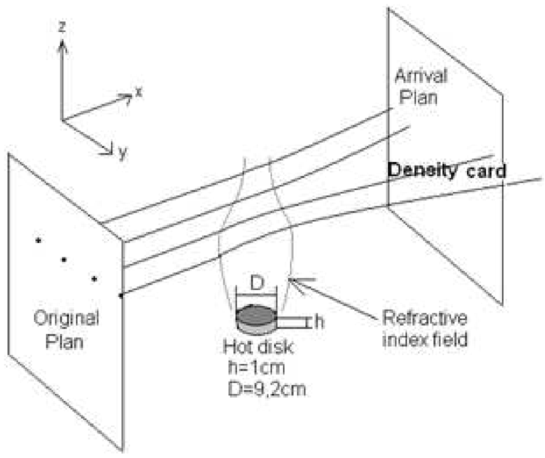

Figure 9: Diagram showing the functioning of the code and its geometry.

The transition from one cell to another is governed by the Snell-Descartes law (transition between a cell i to a cell j with n and θ respectively the refractive index of the cell and the angle between the ray and the normal to the cell surface):

$$n_i \cdot sin(\theta_i) = n_j \cdot sin(\theta_j) \tag{10}$$

Then, when the ray goes out of the last cell, so from the thermal perturbation, it continues his path until the arrival plan, which the position according to x can be adjusted to accentuate the distortion effect. Indeed, the further the screen is, the more the deviation is. We will chose in our example a distance of 37cm. If we discretize sufficiently the original plan and thus enough rays are launched (around

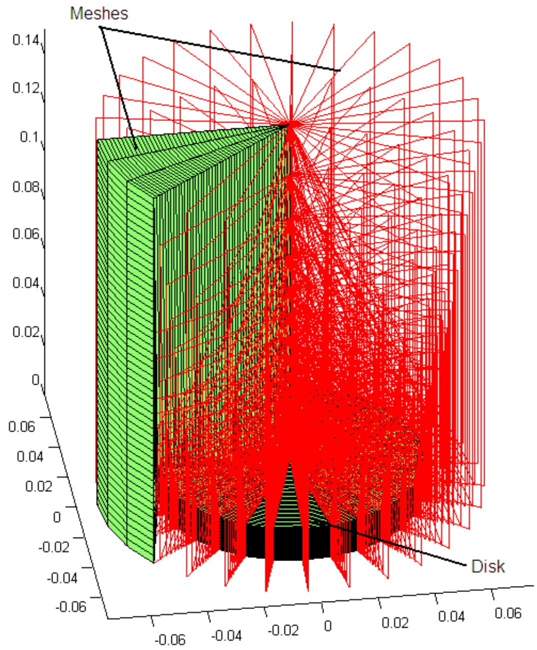

Figure 10: The volume discretisation in cells.

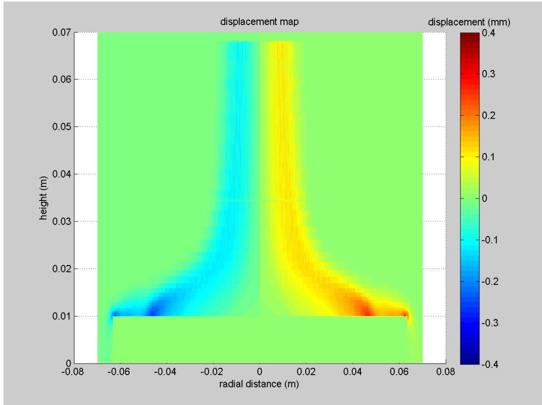

Figure 11: The volume discretisation in cells.

500 000 to obtain the Fig. 11) we obtain on the arrival a displacement map. The most important is to discretize sufficiently the arrival plan because it will affect directly the precision of the displacement. For example, if the arrival plan is 7cmx7cm, and if we discretize it by 1000x1000, the smallest displacement measurable is 0.07mm but thanks to mathematic interpolations we can reach much smaller displacement (0.0001mm). The discretization of the original plan matters mainly about the results visualization and result density. The displacement map obtained permits to quantify the displacement of each ray between the original plan and the arrival one. We can display either the displacement along y, z or the component of both $w=\sqrt(y^2+z^2)$. Results obtained are showed in Fig. 11.

The displacement map shows that the biggest displacements are located along the vertical edges of the disk, in the thermal boundary layer. These zones correspond to the strongest temperature gradient. The displacement on the vertical above the disk can reach around 0.3mm and 0.14mm in the plume. Moreover, in agreement with the Snell-Descartes law, we can notice that we dont have displacement in the center of the plume.

According to results obtained numerically with such set-up (Table 1), and using the proper objective on the camera in order to have a field of view around 10cm, we will be able to obtain displacement big enough to be detected by the detector of the camera:

3.3. *Set-up design*

The disk selected for the experiment has a diameter of 9.2cm with 1cm of thickness. Its made of Inconel 600 and is heated up thanks to a resistance coiled and welded under it. The maximum temperature reachable (to dont deteriorate the welds) is 950°C with a power heating of 1300W. The heating element includes two embedded thermocouples used for regulation and security. The disk will be surrounded of an insulator made of mica paper impregnated with silicone resin under high pressure and temperature. This material has a poor conductivity ($0.27W.m^{-1}.K^{-1}$) and can resist to high temperature up to 800°C. Moreover, to avoid any perturbations coming from the surrounding environment, an enclosure is needed. We chose to realize an enclosure with metallic plates painted in black in order to avoid reflections on the walls (Fig. 12). Different holes are done on its face for future experiments. We can see in the Fig. 12 that the whole enclosure has been included in a second enclosure made of wood to avoid again perturbation coming from the room. The plume is VERY sensible to the out coming variation of pressure. Indeed the pressure variation in the plume is extremely small, around 1 or 2 Pa only.

4. Characterization and tests of the set-up

4.1. *Disk characterization*

The first test performs on the disk was done to verify the stability in time of the temperature and the homogeneity of the disk at the surface. In order to reg-

Type of cameras *Resolution*	**Classical Camera CCD** *1392x1036*				**NIR Camera** *320x256*	**IR Camera** *320x240*
Wavelengths	*200nm*	*400nm*	*632,8nm*	*750nm*	*1μm*	*8μm*
Maximum displacement in the plume (mm)	0,1482	0,1295	0,1267	0,1262	0,1257	0,1241
Maximum displacement above the disk (mm)	0,323	0,2822	0,2761	0,2751	0,2739	0,2705
Plume width 3cm aboce the disk (mm)	43,00	42,34	42,28	42,26	42,24	42,18

Table 1: Displacements expected for each wavelength and width of the plume.

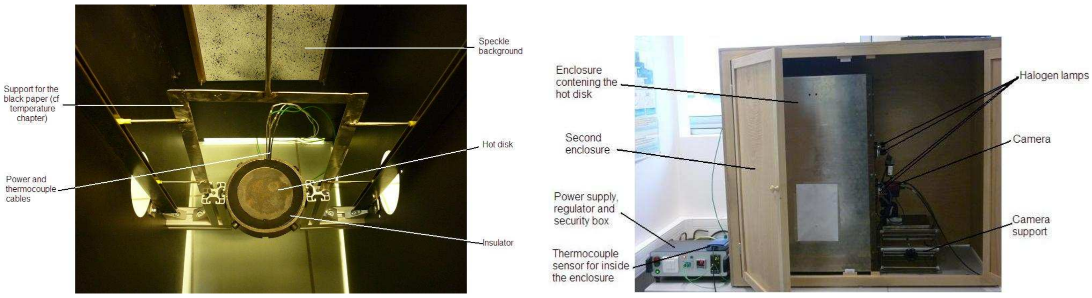

Figure 12: Pictures showing the set-up inside the enclosure and the whole equipment.

ulate the disk and to supply it in power, a PID regulator and a power supply unit are used (Fig. 12). A black paint for high-temperature is applied on the surface in order to have a uniform emissivity, then is observed with an infrared camera during the heating period (Fig. 13). We set the temperature of the resistance at 800°C. The heating element reaches the stability (within 0.1°C) after a slow increase of the temperature (20°C per min) and we get a surface temperature with an average of 800°C and a standard deviation of 18.4°C (if we take a zone of interest smaller than the whole disk, we can reach a much smaller standard deviation).

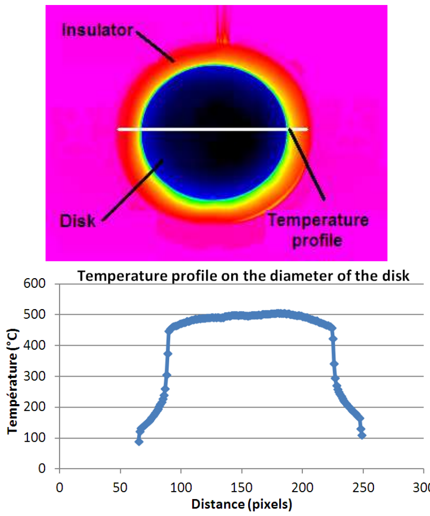

Figure 13: Thermogram and temperature profile of the disk and its insulator at 500°C.

4.2. Plume characterization

4.2.1. Temperature

The plume obtained with this heating element is investigated by means of several methods and is compared with results obtained with FLUENT. The temperature inside the plume is measured by the aim of an infrared camera. We put vertically, in the exact middle of the plume, a sheet of paper painted in black (of known emissivity) and we measure the temperature taken by the paper itself. The paper can be considered as a thermally thin object (Paper Biot number $\approx$0.03$\ll$0.1) which means that the paper will take, in all its depth, the temperature of the fluid in contact. However, the problem of the diffusion appears in this case. Indeed, we can see on the Fig. 16 that that width of the plume is lightly longer than the width of the numerical plume. This diffusion leads to a plume more width and thus a maximum temperature lower. The temperature of the disk has been fixed at 100°C. The numerical and experimental temperature fields are shown respectively in Fig. 14 and 15, and a profile done at a given height (20mm above the disk) is compared with a FLUENT profile in the Fig. 16.

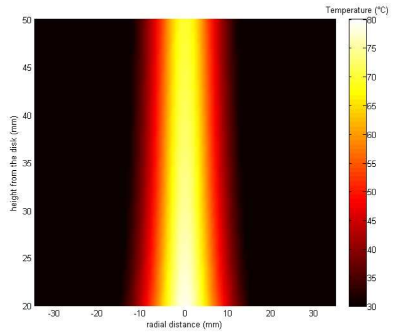

Figure 14: Temperature field obtained with FLUENT.

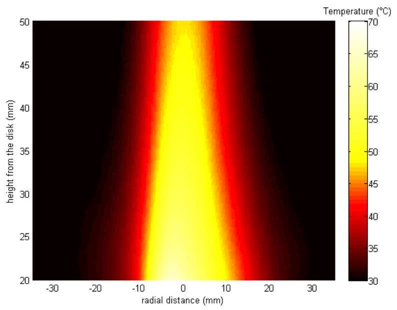

Figure 15: Temperature field obtained with the infrared camera.

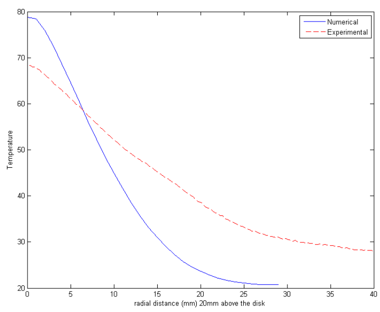

Figure 16: Temperature profiles 20mm above the disk obtained experimentally and numerically.

4.2.2. *Velocity in the plume*

Moreover, a PIV method [12] has been carried out in order to get the velocity field inside the plume and to validate once more FLUENT. The data comparison is displayed in the Fig. 18 and 17.

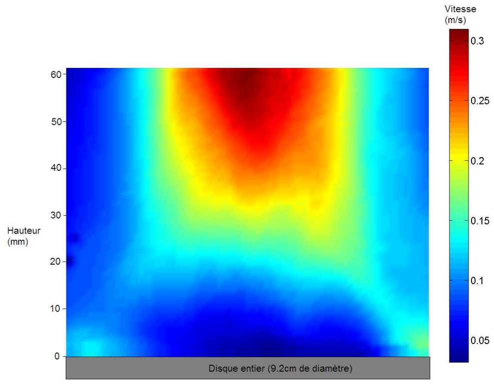

Figure 17: Velocity field obtained with FLUENT.

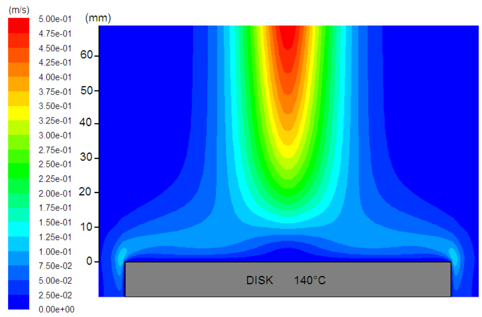

Figure 18: Velocity field obtained by PIV.

If we check in the middle of the plume at 6 cm above the disk, we can find the value of 0.32m/s and 0.45m/s respectively for the experimental and numerical results. The lower speed for the experimental result can be explained by the fact that we were measuring the speed of the seeding and not of the air itself. The ambient air was seeded with very thin drops of oil and its certainly possible that the velocity of the drops, cause of their weight, underestimates the velocity of the air. However, the results obtained (with quite difficulties) show that the order of magnitude remain the same and the velocity fields are similar (experimental results close to the disk are very hard to obtain, thats why the picture is sharper at the top).

4.2.3. *Schlieren photography*

The shape of the plume is explored as well with a schlieren photography technique. Schlieren photography is a visual process that is used to photograph the fluids flow of varying density. The basic optical schlieren system uses light from a single collimated source shining on a target object. Variations in refractive index causes by density gradients in the fluid distort the collimated light beam. the collimated light is

focused with a lens, and a knife-edge is placed at the focal point, positioned to block about half the light. In flow of uniform density this will simply make the photograph half as bright. However in flow with density variations the distorted beam focuses imperfectly and parts which have been focused in an area covered by the knife-edge are blocked. The result is a set of lighter and darker patches corresponding to positive and negative fluid density gradients in the direction normal to the knife-edge.
Several interferential filters has been used in order to see if it was possible to distinguish an enlargement of the diameter between several wavelength (cf Fig. 4) and then to compare it with the one calculated with the ray-tracing (Table 1). But as you can see in this table, the width changes only of 0.8mm in the visible band, too small to be clearly seen by the schlieren photography technique. However, if we check the average width of the plume itself over the different wavelengths with the numerical results we find a length in agreement with an error of few percent with the numerical results. If undisturbed, the plume will be a steady flow whose energy transport rate is equal to the heat transfer rate from the disk surface. Theoretically, the plume width (at a given elevation) should decrease with increased source strength [13]. A example of image taken with this method is shown in the Fig. 19.

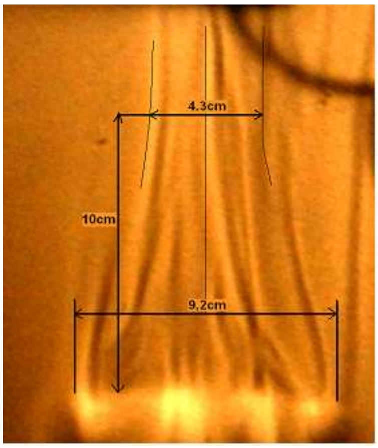

Figure 19: Image of the plume done with the Schlieren photography technique (disk temperature = 650K).

5. Displacements results

To measure the displacements induced by the plume we will use a technique called Background Oriented Schlieren (BOS) [14]. Background Oriented Schlieren is a novel technique for flow visualization of density gradients in fluids using the Gladstone-Dale relation between density and refractive index of the fluid. BOS simplifies the visualization process by eliminating the need for the use of expensive mirrors, lasers and knife-edges. In its simplest form, BOS makes use of simple background patterns of the form of a randomly generated dots, speckle image. In its initial stages of implementation, it was mostly being used as a qualitative visualization method. But in our case, thanks to a correlation software, we are able to obtain a quantitative displacement. The Fig. 20 gives the working of the BOS method:

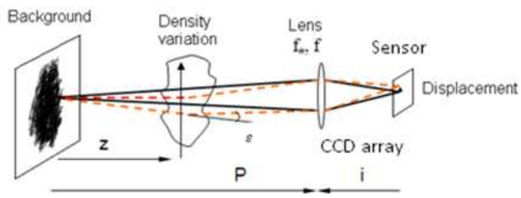

Figure 20: Diagram explaining the BOS technique.

To obtain result of displacement, two images of the background are recorded, one with perturbation and one without. Then, an analysis of these images is made in order to deduct the displacement of each element from the dot-pattern. This analyze is realized with the help of the software VIC2D [15]. It makes a correlation between the two pictures and gives as result the displacement of each element in pixel along the *x* direction and *y* direction. The displacement measured by the camera is directly linked to its distance with the plume. The distance **Z** is fixed at 30cm and **P+I** at 67cm (cf Fig. 20).

5.1. *Visible*

The camera used is a Pike F-145B/C with Sony ICX285 CCD sensor. The sensor resolution is 1388x1038 and works efficiently between 400nm and 800nm. We used an objective with a focal distance of 25mm which allowed us to explore around 10cm width in the plume few milimeters above the disk. With such set-up and with a disk heated up to 800°C, we obtained the following displacement field:

The Fig. 21 shows clearly the perturbation produced by the presence of the plume created by the hot disk. As expected, a deviation of rays of light occurs on the right side (displacement in the *x* direction) and left side (displacement inverse to the *emphx* direction) of the plume whereas the center of the plume

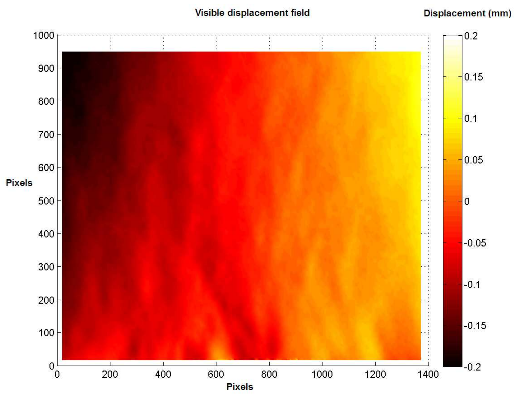

Figure 21: Displacement field in the visible band (average figure over 20 images.

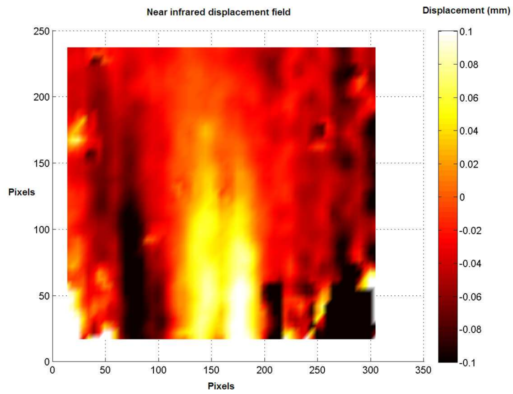

Figure 22: Displacement field in the NIR band (average figure over 10 images.

keeps a displacement very close to 0. If we compute the mean of the maximum displacement over all the pictures taken (600), we obtain a displacement of 0.27mm which is in good agreement with the numerical result (Table 1). The difference between the numerical and experimental results are lower than 5%.

5.2. Near infrared

For the near infrared band, we will use a XenICs camera XEVA-FOA-1.7-320, with a InGaAs Sensor. This sensor of 320x256 is working exceptionally in the range of 400nm - 1700nm. We had to insert between the objective and the density variation a filter in order to cut off the visible spectral band. The filter from Optosigma company cuts 100% of rays under 850nm. The focal length of the objective used in this case, cause of the lower resolution, is 50mm which permit to have 6cm of the plume in the field of view. The interest zone in pixel is 290x225.

In the Fig. 22 , we can still located the center of the plume between the two zones of positive and negative displacements (red and blue). The lowest displacement upper in the plume doesnt appear clearly with such camera because of the weak resolution of the sensor (even though we used a longer focal length). But we can still distinguish easily the perturbation occurring close of the disk. The two bottom corners of the figure have to be ignored because of correlation problems in this zone, as well as some blue and red points in the plume, corresponding with dead pixels. If we realize a window of interest on the plume itself and that we compute the average of the maximum displacement over 600 pictures, we obtain a value of 0.24mm. This result is in agreement with the numerical one, with 12% difference.

5.3. Infrared

For the infrared measurement, we used a FLIR SC325 camera. The microbolometric sensor working between 7.5 and 14μm (and -20°C up to +1200°C) has a resolution of 320x240 pixels. The objective used for the experiment has a focal length of 30mm, giving us the possibility to have 10cm (width) of field of view in the plume. The background observed with the camera in this case was different as before. We created a IR pattern [16] thanks to a copper plate painted in black and heated ($\approx$ 250°C) by a MICA resistance, and an aluminum plate pierced with holes (Fig. 23). The pattern is smaller than the field of view of the camera (to short focal length or to small pattern) and thats why the Fig. 24 is only a matrix of 175x140.

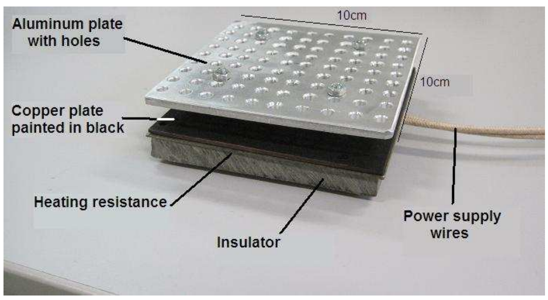

Figure 23: Pictures of the IR pattern created for the experiment.

As we can guess, the density results with such pattern is inferior than with a speckle image. Nevertheless, thanks to the interpolations made by the software VIC2D, we can obtain a result quite similar. We notice however somevertical bands on the pictures which actually correspond with zones without holes. We see on the Fig. 24 a part of the plume (around 5cmx4cm)

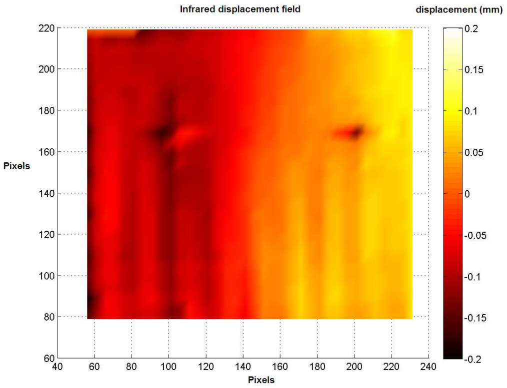

Figure 24: Displacement field in the NIR band (average figure over 10 images.

with no displacement in the center and respectively a positive and negative displacement on the right and left side of the plume. The displacement is slightly inferior than in the previous case because the picture has been taken a little upper in the plume. Indeed, the bottom of the pattern was loosing of contrast with time because it was getting more hot with the disk radiation. The average max displacement computed here is 0.153mm, still in agreement with the numerical results obtained in the plume. The two blue points on the picture correspond on the screws used to hold the aluminum plate with heating element.

6. Conclusion and perspectives

The work done here has pointed out the mirage effect phenomena in several spectral bands and we gave quantitative information about the displacement induced by the perturbation. We showed, thanks to an original set up allowing measurement in all the cameras spectral bands, that the displacement was around 0.26mm close to the disk and about half of it in the plume. The variation of the refractive index is essentially due to the temperature gradient (compare with the wavelength) and thus the displacements observed in any spectral bands are slightly the same. The main problem to be able to compare the experimental results is the weak resolution of sensor in the near infrared and infrared spectral bands. Indeed, the camera has to be far enough of the perturbation (or longer focal length should be used) to allow a measurement of the displacement. In our case, a strong temperature gradient and a focal length big enough gave us interesting results. We also brought out that the displacement generated by the axisymmetric plume was predictable by our ray-tracing tool (and by the preliminary use of a CFD software). Many experiments has be carried out in order to validate the numerical method such as infrared thermography, particle image velocimetry, schlieren photography. Although the preliminary experiences were tending to underestimate the Fluent results, the final measurements with background oriented schlieren are inclined to prove the accuracy of the numerical method.

The next step will be to correct pertubated images and to obtain images without perturbation coming from refractive index gradient. In the case of a laminar convection, the ray-tracing code can be used to predict the deviation of each point since we know the perturbation. If we don't know the perturbation but keeps axisymmetric proprieties, a method is in progress in order to retrieve the 2D index refractves field from the displacement given by the BOS [17; 18]. The 2D index refractives field is then transofrmed in 2D axisymmetric field thanks to the inverse Abel transform [19]. In the case of a turbulent flow, a statistical approach [20] and/or treatment of images by an algorithm [21; 22] seem to be more appropriate in an attempt to correct images.

References

[1] Healey G. E., Kondepudy R. - *Radiometric CCD Camera Calibration and Noise Estimation*, IEEE Transaction on pattern analysis and machine intelligence, vol.16, no.3, March 1994

[2] Claudinon S. - *Contribution l'tude des distorsions au traitement thermique*, Thse Ecolde des Mines de Paris, 2000

[3] Bing P., Dafang W., Yong X. - *Hight-temperature deformation field measurement by combining transient aerodynamic heating simulation system and reliability-guided digital image correlation*, Optics and Lasers in Engineering 48, pp 841-848, 2010

[4] De Strycker M., Schueremans L., Van Paepegem W., Debryne D. - *Measuring the thermal expansion coefficient of tubular steel specimens with digital image correlation techniques*, Optics and Lasers in Engineering 48, pp 978-986, 2010

[5] Lyons J.S., Liu J., Sutton M.A. - *High-temperature deformation measurements using digital image correlation*, Experimental Mechanics, March 1996

[6] Grant B.M.B., Stone H.J., Withers P.J., Preuss M. - *High-temperature strain field measurement using digital image correlation*, The Journal of Strain Analysis for Engineering Design May 1, 2009

[7] Cosson B., Schmidt F., Le Maoult Y., Bordival M. - *Infrared heating stage simulation of semi-transparent media (PET) using ray-tracing method*, International Journal of Material Forming, vol.4, n1, p1-10, 2011

[8] Mayinger F., Feldmann O. - *Optical measurements* 2^{nd} *Edition*, Springer, 2001

[9] Lide D. R. - *Handbook of Chemistry and Physics* 88^{th}, 10-253, 2007-2008

[10] Crespy C. - *Contribution la mesure de champs de temprature bi et tri-dimensionnels par Photographie de Speckle. Applica-*

tion lestimation des flux d chaleur paritaux, PhD thesis INSA Lyon, 2009

[11] El Motassadeq A., Chechouani H., Waqif M., Benet S. - *Simulation des effets de la rfraction dans la couche limite thermique au-dessus d'un disque horizontal*, Congrs franais de thermique, 2000

[12] Scarano F., Carlomagno G.M., Riethmuller M.L. - *Particle Image Velocimetry Development and Application*. Rhode Saint Genese: Von Karman Institute for Fluid Dynamics, 2000

[13] Robinson S. B., Liburdy J. A. - *Prediction of the natural convective heat transfer from a horizontal heated disk*, Journal of Heat Transfer, vol. 109, November 1987

[14] Klinge F. - *Investigation of background oriented schlieren towards a quantitative density measurement system*, Project report, von Karman Institute, 2001

[15] VIC-2D, Correlated Solutions Inc., http://correlatedsolutions.com.

[16] Saint Laurent L., Prvost D., Maldague X. - *Fast and accurate calibration-based thermal / colour sensors registration*, QIRT 2010-126.

[17] Klinge F. - *Investigation of background oriented schlieren towards a quantitative density measurement system*, project report 19, Von Karman Institute, 2001

[18] Sourgen F., Haerting J, Rey C. - *mesure de champ de masse volomique par Background Schlieren Displacement (BSD)*, Institut Franco-allemand de Recherches de Saint Luis, 2003

[19] Dibrinski V., Ossadtchi A., Mandelshtam V., Reisler H. - *Reconstruction of Able transformable images: the gaussian basis-set expansion Abel transform method*, Review of scientific instruments, Volume 73 number 7, 2002

[20] Rondeau X. - *Imagerie travers la turbulence : mesure inverse du front donde et centrage optimal*, PhD thesis, Lyon University, 2007

[21] Thorpe G., Fraser D. - *Correction and restoration of images obtained through turbulent media*, Digital signal processing applications, pp 415-420, 1996

[22] Lemaitre M., Lalignant O., Blanc-Talon J., Meriaudeau F. - *Local isoplanatism effects removal on infrared sequences*, Proceedings of SPIE, Quality Control by Artificial Vision (QCAV) Conference, France, Vol. 6356, 2007